The Journal of Experimental Biology 203, 2603–2622 (2000)
Printed in Great Britain © The Company of Biologists Limited 2000
JEB2753

LIMITS TO OPTIMIZATION: FLUID DYNAMICS, ADHESIVE STRENGTH AND THE EVOLUTION OF SHAPE IN LIMPET SHELLS

MARK W. DENNY*

Stanford University, Hopkins Marine Station, Pacific Grove, CA 93950, USA

*e-mail: mwdenny@leland.stanford.edu

Accepted 6 June; published on WWW 9 August 2000

Summary

Limpets are commonly found on wave-swept rocky shores, where they may be subjected to water velocities in excess of 20 m s^{-1}. These extreme flows can impose large forces (lift and drag), challenging the animal's ability to adhere to the substratum. It is commonly thought that the conical shape of limpet shells has evolved in part to reduce these hydrodynamic forces while providing a large aperture for adhesion. This study documents how lift and drag actually vary with the shape of limpet-like models and uses these data to explore the potential of hydrodynamic forces to serve as a selective factor in the evolution of limpet shell morphology. At a low ratio of shell height to shell radius, lift is the dominant force, while at high ratios of height to radius drag is dominant. The risk of dislodgment is minimized when the ratio of height to radius is 1.06 and the apex is in the center of the shell. Real limpets are seldom optimally shaped, however, with a typical height-to-radius ratio of 0.68 and an apex well anterior of the shell's center. The disparity between the actual and the hydrodynamically optimal shape of shells may be due to the high tenacity of limpets' adhesive system. Most limpets adhere to the substratum so strongly that they are unlikely to be dislodged by lift or drag regardless of the shape of their shell. The evolution of a tenacious adhesion system (perhaps in response to predation) has thus pre-empted selection for a hydrodynamically optimal shell, allowing the shell to respond to alternative selective factors.

Key words: limpet, shell morphology, hydrodynamic force, optimization, evolution, lift, drag.

Introduction

The coiling characteristic of most gastropod shells (Vermeij, 1993) is greatly reduced in limpets (the Patellogastropoda), resulting in a conical shell with a large aperture. However, there is substantial variation on this theme. Some limpets' shells (such as that of *Acmaea mitra*) are very high-spired, with a height-to-length ratio that exceeds 0.6. Others (such as *Tectura scutum* and *Patella ocularis*) have height-to-length ratios of less than 0.2. The apex in many limpets is close to the center of the shell, but in a few cases (such as *Lottia digitalis*, *Lottia gigantea* and *Helcion petunculus*), the apex may actually overhang the anterior edge of the shell.

A variety of functional interpretations and evolutionary scenarios have been assigned to the differences among limpet shell shapes (for reviews, see Branch, 1981; Vermeij, 1993). These include the possibility that shell shape has evolved in response to thermal and desiccation stress in the intertidal zone, predation on limpets by crabs (Lowell, 1985, 1986, 1987) and birds (Hahn and Denny, 1988), and foraging and territorial behavior by the limpet itself (Stimson, 1970). Recently, D. R. Lindberg and W. F. Ponder (in preparation) have suggested that the shape of limpets' shells may have evolved in response to reduced oxygen availability: low-spired shells allow for a larger gill. The existence and relative contribution of these factors have been debated.

Many limpet lineages evolved on wave-exposed rocky shores where animals are subjected to water velocities that can exceed 20 m s^{-1} (Denny et al., 1985; Denny, 1988, 1995). These extreme flows can impose large forces, testing the organism's ability to adhere to its rocky substratum, and it is commonly accepted that shell shape in limpets has evolved (at least in part) to minimize hydrodynamic forces while providing a large aperture for adhesion to the rock (Branch, 1981; Denny, 1988; Vermeij, 1993). The present study documents how hydrodynamic forces actually vary with the shape of limpet-like models and uses these data to explore the potential of hydrodynamic forces to serve as a selective factor in the evolution of shell shape in limpets.

Several studies have addressed the role of shell shape in determining the hydrodynamic force to which a limpet will be subjected (e.g. Warburton, 1976; Branch and Marsh, 1978; Denny, 1985, 1988, 1989, 1995), but each has been severely limited. In most cases, the only force measured was drag (a force in the direction of flow); lift (the force perpendicular to flow) was neglected. Denny (1989, 1995) measured lift on a variety of limpet species and suggested that in many cases lift is a larger force than drag. Unfortunately, the apparatus used to measure lift was less than ideal (see Materials and methods: lift and drag from direct measurements), and the accuracy of

these measurements is therefore suspect. Denny (1988) reported indirect measurements of lift and drag on model limpet shells and used these to calculate the torques exerted on shells and the consequent tensile force transmitted to the glue beneath a limpet's foot. These calculations suggested that there is an optimal shape for limpet shells that minimizes the risk of dislodgment relative to the volume of body enclosed by the shell. Unfortunately, the mechanics of the situation were formulated incorrectly (the limpet was treated as a bent beam), and these results are also suspect.

This study attempts to circumvent these limitations. Through the use of physical models, the lift, drag, center of lift and center of drag have been measured for cones of a range of shapes that encompasses those found in limpets. These measurements allow for a calculation of how the risk of dislodgment varies as a function of shell shape and for an assessment of the relative magnitudes of shear and tensile stress in the glue by which limpets adhere to the substratum. In the light of these analyses, a general conclusion emerges. The shape of limpet shells is 'good enough' to keep applied hydrodynamic forces within the bounds set by the animals' adhesive system, but the selection pressure due to flow-induced mortality has not been sufficient to optimize the shells' lift and drag coefficients. It is perhaps surprising that limpets, living in one of the most extreme flow regimes on earth, apparently have a shell shape that is not finely tuned to that physical environment. If this is indeed true, the shape of limpet shells provides a case study illustrating the limits to optimization through natural selection and the consequences when competing selective factors operate on the same structure.

Materials and methods

Lift and drag

At the high flow velocities characteristic of wave-swept rocky shores, the lift, L, imposed on a limpet can be modeled using the standard equation (Denny, 1988; Vogel, 1994):

$$L = p_d A_{pl} C_L , \quad (1)$$

where A_{pl} is the planform area of the limpet (its shell area projected perpendicularly onto the substratum, essentially the aperture area) and C_L is the dimensionless coefficient of lift. Here, p_d is the dynamic pressure, the pressure the moving fluid would exert if it were brought to a complete stop:

$$p_d = \tfrac{1}{2}\rho u^2 , \quad (2)$$

where ρ is the density of the fluid and u is the fluid's velocity relative to the organism. Similarly, drag, D, can be modeled as:

$$D = p_d A_{pr} C_D . \quad (3)$$

Here, A_{pr} is the area projected onto a plane perpendicular to flow and C_D is the dimensionless drag coefficient.

The measurements of C_L and C_D reported here were carried out in a wind tunnel (Denny and Gaylord, 1996); thus, the fluid density in the above equations is that of air (1.2 kg m^{-3} at 20 °C). The shift from water (the medium most relevant to limpets) to air is permissible when measuring lift and drag coefficients provided that the Reynolds number is held constant (Vogel, 1994). Reynolds number, Re, is uy_c/ν, where u is again the fluid's velocity, y_c is a characteristic length (here taken to be the length of the object in the direction of flow) and ν is the kinematic viscosity of the fluid in question (Vogel, 1994). At 20 °C (the temperature of these experiments), the kinematic viscosity of air is 15.1×10^{-6} m^2 s^{-1} and that of sea water is 1.06×10^{-6} m^2 s^{-1} (Denny, 1993). Thus, for fluids at this temperature and an object of a given size, the Reynolds number in air is the same as that in water if the velocity of the air is 14.2 times that of the water. If the temperature of sea water is 10 °C (a common value on temperate shores), its kinematic viscosity is 1.35×10^{-6} m^2 s^{-1}, and at constant Re the ratio of air velocity (at 20 °C) to water velocity is 11.2.

Accelerational force

In addition to drag and lift, limpets are exposed to a force proportional to the water's acceleration (Batchelor, 1967; Denny, 1988), but this force will not be considered here. The accelerational force varies with the volume of water displaced by an organism, and for the diminutive size of most limpets it is small compared with lift and drag, even given the extremely rapid accelerations present in the surf zone (Denny, 1989). Furthermore, Gaylord (1997, 2000) has shown that, while rapid accelerations are common on wave-swept shores, the spatial scale of acceleration is quite small (1 cm or less). As a consequence, even if a large limpet displaces a substantial volume of water, acceleration will not be coherent over the entire animal, and the accelerational force will still be small.

Measurement of dynamic pressure

During each experiment, the dynamic pressure of the wind was measured using a manometer attached at one end to a Pitot tube and at the other end to a static port. The Pitot orifice was orientated upstream 14 cm from the tunnel wall (outside the tunnel's boundary layer), and the static orifice was located in the tunnel wall well upstream of the model. The dynamic pressure was calculated as:

$$p_d = \boldsymbol{g}\rho_{eff} S \sin\theta , \quad (4)$$

where ρ_{eff} is the effective density [the difference in density between the 95 % alcohol used as the manometer fluid (804 kg m^{-3} at 20 °C) and the density of air (1.2 kg m^{-3} at 20 °C)] and $\boldsymbol{g}$ is the acceleration due to gravity. S is the deflection (in m) of the meniscus along the manometer tube (measured from its control position in the absence of the experimentally applied pressure), and θ is the angle of the manometer from the horizontal. The dynamic pressure can be used to calculate the mainstream wind velocity:

$$u = \sqrt{\frac{2p_d}{\rho_{air}}} , \quad (5)$$

where ρ_{air} is the density of air.

Models

Five right cones (referred to here as 'symmetrical' cones) were turned from acrylic plastic, each with a diameter of approximately 5 cm and heights as shown in Table 1. These cones were used both in the direct measurement of drag and lift and in the measurement of the flow-induced pressure imposed on a fluid beneath each cone in flow. A second, nominally identical, set of cones was turned, into which ports were drilled for the measurement of pressure distributions. Between 16 and 20 ports (each 0.6 mm in radius) were drilled along a diameter of the cone; the ports on opposite sides of the apex differing in their distance from the apex (Fig. 1). The basal end of each port was connected *via* flexible tubing to its own manometer (see below).

Two additional models were constructed by slicing symmetrical cones in a plane that was not perpendicular to the cone's axis. The apex of the resulting shapes was thus displaced from the center, and these asymmetrical cones (Table 1; Fig. 2) resemble a variety of limpet shells. For these asymmetrical cones, 'peakedness' is measured as the ratio of the height to half the length in the direction of flow. The relative location of the apex is expressed by E:

$$E = \frac{d_a}{(\lambda/2)}, \qquad (6)$$

where d_a is the distance to the apex from the anterior edge of the model and λ is the overall length of the model. The distance to the apex and the length of the model are both measured in the planform projection of the model rather than on the model's surface, with the result that E is equal to 1 for a centrally located apex and is less than 1 for an apex located anterior to the center. Pressure ports (48–52) were drilled at closely spaced intervals covering the circumference and upper surface of these shapes, and each port was connected to a separate manometer (see below).

Pressure distributions

The pressure distribution over the models was measured in the wind tunnel at an air velocity of 29 m s^{-1}, giving a Reynolds number equal to that of sea water moving with a velocity of 2.0–2.6 m s^{-1} (depending on the temperature of the water). The boundary layer in the tunnel was typical of turbulent flow (such as that found on wave-swept rocky shores) and is described in detail by Denny and Gaylord (1996). Each model 'limpet' was mounted on a flat, circular plate that fitted into a circular opening in the tunnel wall. Once in position, the inner surface of the plate (and hence the base of the model) was flush with the inner surface of the tunnel wall. The orientation of the model relative to the wind could be varied by rotating the circular plate. This

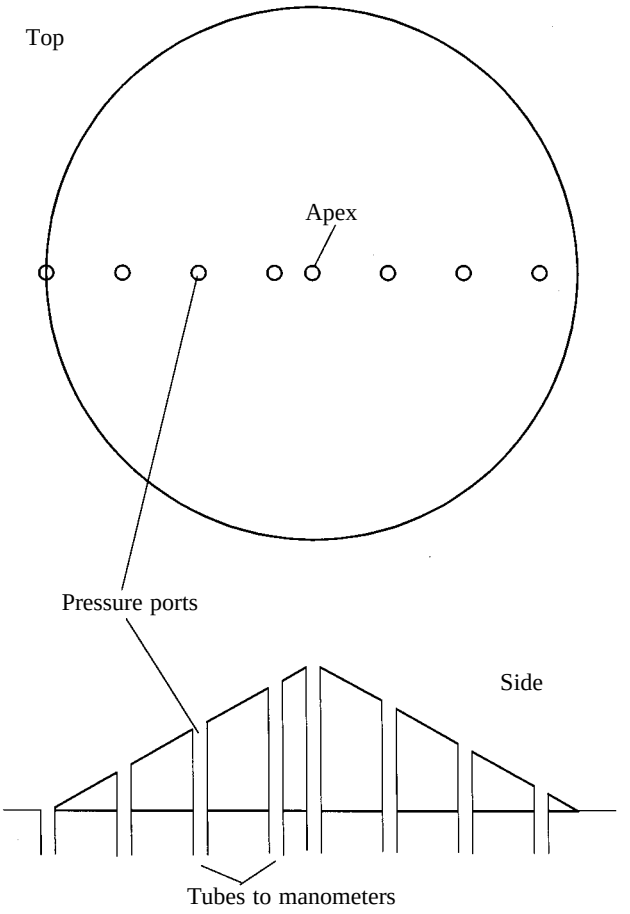

Fig. 1. A schematic diagram of the arrangement of pressure ports on an experimental right (symmetrical) cone. Not drawn to scale. In the actual models, there were 16–20 ports.

Table 1. *Dimensions of the models used in these experiments*

Cone	Height (cm)	Diameter or length (cm)	Width (cm)	H/R (or $\frac{H}{\lambda/2}$ for asymmetrical cones)	$\frac{H}{W/2}$	E
1	3.64	5.03		1.45		1.00
2	3.03	5.01		1.21		1.00
3	2.41	4.95		0.97		1.00
4	1.38	4.86		0.57		1.00
5	0.74	4.90		0.30		1.00
Asymmetric 1	2.11	4.46	4.35	0.95	0.97	0.70
Asymmetric 2	1.37	3.61	3.21	0.76	0.85	0.38

H, height; W, width; λ, length in the direction of flow; R, radius; E, proportional location of shell apex (see equation 6).

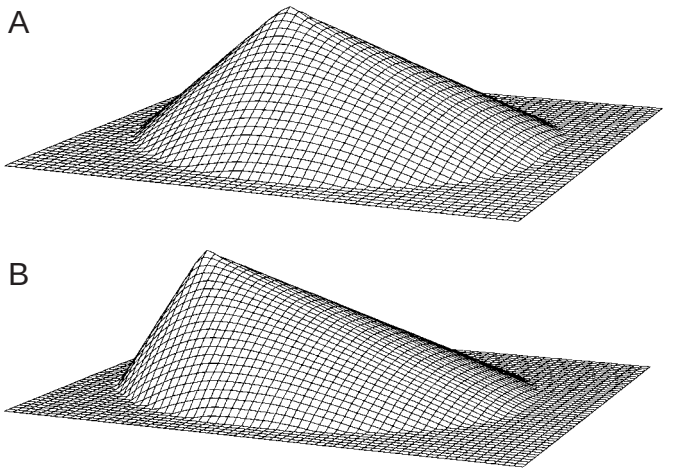

Fig. 2. Perspective drawings of (A) the less asymmetrical cone (asymmetric 1 in Table 1) and (B) the more asymmetrical cone (asymmetric 2 in Table 1) used in these experiments.

allowed for a detailed measurement of the pressure distribution on the symmetrical cones by rotating the line of pressure ports through a series of angles between 0° and 180°. Increments of 10° were used, providing direct measurements of pressure at 304–388 points over the cone's surface and (given the symmetry of the cones) effective measurements at 576–720 points.

Pressure ports on the models were connected to a bank of manometers, as shown in Fig. 3. The tube from each port transmitted the experimental pressure to the top of a glass manometer. The bottom of each manometer was connected to a large-bore manifold, which in turn was connected to a reservoir containing alcohol. The height of the reservoir set the control level of the meniscuses in the bank of manometers, and the height of the meniscus in each manometer tube varied in response to the experimentally applied pressure. The sensitivity of the apparatus could be varied by tilting the plane of the manometer bank away from the vertical; the more horizontal the plane, the larger the excursion of each meniscus for a given applied pressure (see equation 4). The angle of the manometer bank was measured using an electronic level (SmartLevel, Wedge Innovations, Inc.), and the surface area of the reservoir (0.11 m^2) was sufficiently large that the control height varied negligibly as individual meniscuses moved up and down during an experiment. The location of the meniscus in each manometer was recorded using a digitizing pad (Numonics model 2200) mounted immediately behind the bank of manometers. During an experiment, the height of each meniscus was digitized 10–20 times, and the average of these values was used to estimate pressure *via* the manometer equation (equation 4). Pressures acting on the asymmetrical cones were measured as for the symmetrical cones, but all pressure ports were measured simultaneously while the model was held in a particular orientation (apex upstream, downstream, or at 90° to the flow).

Lift and drag from pressure measurements

The pressure measurements described above provide an

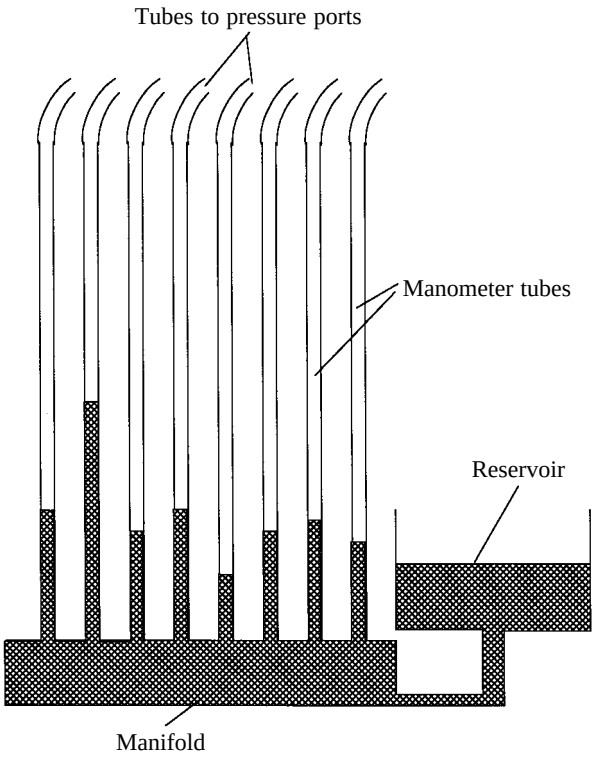

Fig. 3. A schematic drawing of the manometers used to measure the pressure distribution over models. Not drawn to scale.

estimate of the pressure distribution over the models. This pressure distribution can subsequently be used to calculate the lift and pressure drag acting on the model as follows. First, the pressures measured at the ports are used to estimate the pressures acting at a grid of points projected onto the planform area of the model. The transformation from the radial (for the symmetrical cones) or haphazard (for the asymmetrical cones) array of pressure ports to this orthogonal grid was carried out using Surfer software (version 5.0, Golden Software). The net result is a three-dimensional array [$x(i,j)$, $y(i,j)$, $p(i,j)$] consisting of the Cartesian coordinates of the grid nodes on the planform [$x(i,j)$, $y(i,j)$] and the associated pressure $p(i,j)$. An example of a portion of this type of array is shown in Fig. 4. The indices i and j denote the column and row (respectively) of the grid nodes. A similar array was constructed to describe the three-dimensional topography of the model [$x(i,j)$, $y(i,j)$, $z(i,j)$], where z is the surface elevation of the model at each grid node (measured from the horizontal plane of the model's base) and the nodes have the same locations as for the pressure array. The y axis is parallel to the flow.

The local tilt of the model's surface is estimated for each grid node [$x(i,j)$, $y(i,j)$] as:

$$\frac{\partial z}{\partial x} \approx \frac{z(i+1,j) - z(i-1,j)}{2\Delta x}\,, \tag{7}$$

$$\frac{\partial z}{\partial y} \approx \frac{z(i,j+1) - z(i,j-1)}{2\Delta y}\,, \tag{8}$$

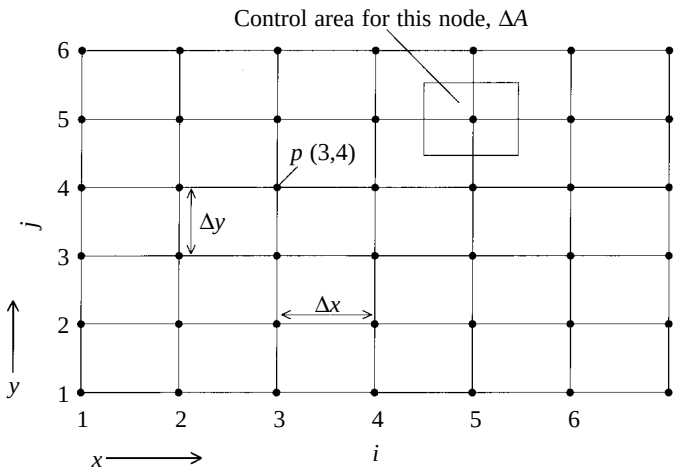

Fig. 4. The type of orthogonal grid used in the calculation of lift, drag and the centers of lift and drag. The grid shown here is one small segment of the much more extensive grid that covers the entire planform area of the model being measured. For a typical model, the overall grid contains 2500–3000 nodes. *x*, *y*, Cartesian coordinates of the grid nodes; *p*, pressure; *i*, *j*, indices denoting the column and row, respectively, of the grid nodes; Δx, Δy are the *x* and *y* spacings between grid nodes, respectively.

where Δx and Δy are the *x* and *y* spacings between grid nodes, respectively (Fig. 4). This tilt is assumed to apply to a rectangular planform area centered on the grid node: $x(i,j)-(\Delta x/2)<x<x(i,j)+(\Delta x/2)$, $y(i,j)-(\Delta y/2)<y<y(i,j)+(\Delta y/2)$. The planform area is thus $\Delta x\Delta y$. In the plane of the model's surface, however, the actual area over which pressure acts at a given node is ΔA (Schey, 1973):

$$\Delta A = \Delta x \Delta y \sqrt{1 + \left(\frac{\partial z}{\partial x}\right)^2 + \left(\frac{\partial z}{\partial y}\right)^2} . \quad (9)$$

The pressure-induced force (ΔF) acting at this grid node is the product of ΔA and the local pressure:

$$\Delta F = \Delta A p(i,j) , \quad (10)$$

and this force acts normal to the plane of the area. As a result, because of the local tilt of the surface, the vector ΔF may have a component along the *x*, *y* or *z* axis. A consideration of the geometry of the situation (Schey, 1973) leads to the following conclusions. The component of ΔF that is parallel to the flow is, by definition, a drag, and when the flow is parallel to the *y* axis:

$$\Delta D = \frac{-\Delta F \left(\frac{\partial z}{\partial y}\right)}{\sqrt{1 + \left(\frac{\partial z}{\partial x}\right)^2 + \left(\frac{\partial z}{\partial y}\right)^2}} . \quad (11)$$

This represents the contribution to the overall drag from one small area of the model. Similarly, the component of ΔF normal to the base of the cone is a lift:

$$\Delta L = \frac{\Delta F}{\sqrt{1 + \left(\frac{\partial z}{\partial x}\right)^2 + \left(\frac{\partial z}{\partial y}\right)^2}} , \quad (12)$$

and this is the contribution to the overall lift from one small area. For the asymmetrical cones oriented broadside to the flow, there may be a lateral lift force, *Q*, in the plane of the wall:

$$\Delta Q = \frac{-\Delta F \left(\frac{\partial z}{\partial x}\right)}{\sqrt{1 + \left(\frac{\partial z}{\partial x}\right)^2 + \left(\frac{\partial z}{\partial y}\right)^2}} . \quad (13)$$

In general, the pressure on the upstream face of an object (which acts to push the object downstream) is greater than the pressure on the object's downstream face (which acts to push the object upstream). The resulting upstream–downstream inequality in pressure-induced force is calculated for the models used here by summing the ΔD forces over all grid nodes, thereby yielding the overall pressure drag, *D*:

$$D = \sum_{\text{all } j} \sum_{\text{all } i} \Delta D(i,j) . \quad (14)$$

Similarly, summing the ΔL forces over all grid nodes yields the gross lift on the object's upper surface, L_g.

$$L_g = \sum_{\text{all } j} \sum_{\text{all } i} \Delta L(i,j) . \quad (15)$$

Just as the overall drag on the model is a result of the difference in pressure between the upstream and downstream surfaces, the net lift acting on the model is due to the difference in pressure between the upper surface of the model and the pressure acting on the model's basal area (the area in contact with the wall). Here, I assume that the pressure on the model's basal area is uniform across the base, and is equal to p_b, the average pressure acting at the basal edge of the model (the line where the model's upper surface contacts the wall). The net lift is thus:

$$L = L_g - A_{pl} p_b . \quad (16)$$

It will be shown that this estimation leads to the calculation of net lift forces that are close to those measured directly.

The total lateral lift, *Q*, is:

$$Q = \sum_{\text{all } j} \sum_{\text{all } i} \Delta Q(i,j) . \quad (17)$$

Direct measurement of pressure under cones

The average basal pressure acting on cones in flow was measured using the apparatus shown schematically in Fig. 5. With the exception of the lowest-spired cones, each

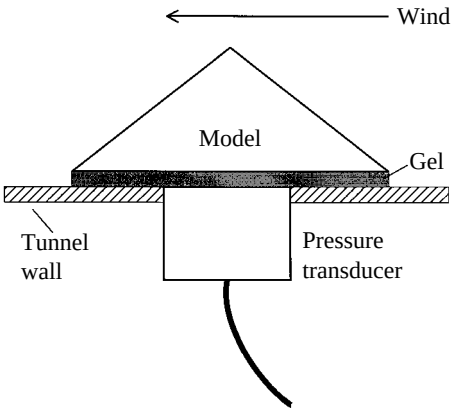

Fig. 5. A schematic diagram of the apparatus used to measure the static pressure under a model cone in flow.

symmetrical cone was rigidly attached to the wall of the wind tunnel with its base centered over a pressure transducer (Omega PX102). The diaphragm of this transducer (1.9 cm diameter) was flush with the inner surface of the tunnel wall. Small plastic spacers maintained a gap of 0.7 mm between the base of the model and the transducer's diaphragm, and this space was filled with a water-soluble gel (K-Y Jelly, Johnson and Johnson Co.). The gel served to simulate the body of a limpet by prohibiting flow beneath the model, but allowed for the transmission of static pressures to the pressure transducer. The voltage output of the transducer was low-pass-filtered and recorded on a strip-chart recorder. The transducer was calibrated by comparing its voltage output with the pressures measured by an alcohol manometer when both were attached to a common pressure source. The extremely thin edges of the lowest-spired cone rendered it impossible to mount it adequately above the pressure transducer, and measurements were therefore not conducted on this cone.

Lift and drag from direct measurements

Drag acting on models was measured using the cantilever-type, dual-beam, strain-gauge force transducer described by Denny and Gaylord (1996). The model was mounted on a flat plate attached to the force transducer, and the transducer was in turn mounted on a wall of the wind tunnel such that the inner surface of the plate (and hence the base of the model) was flush with the tunnel's wall. The voltage output from the transducer (proportional to force) was low-pass-filtered to attenuate fluctuations due to turbulence and recorded on a strip-chart recorder. The recordings were subsequently measured using Vernier calipers, and averages were calculated and converted to force. The device was calibrated by orienting it such that the sensitive axis of the transducer was vertical; accurately known weights were then hung from the transducer. All drag measurements were adjusted for the slight friction drag acting on the exposed portions of the force platform.

Direct measurement of lift on limpet-like shapes is complicated by the fact that the pressure beneath an object adjacent to a wall can be strongly affected by the distance between the object and the wall. In a typical arrangement (such as that used by Denny, 1989, 1995), a model would be held in place by a narrow rod passing through a hole in the wall of the wind tunnel, and the rod (oriented perpendicular to the wall) would couple the lift force acting on the model to the lift transducer. Unfortunately, standard force transducers measure force by measuring the displacement of a beam. As a consequence, when using a transducer of this sort, the model's base must be separated from the wall by a gap sufficient to allow the transducer to deflect freely. It was found that the dimension of this gap had a substantial effect on the lift measured (probably because of fluctuations in pressure in the gap as air flowed through).

To circumvent this problem, a nulling lift transducer was constructed as shown in Fig. 6. The model was suspended from a rod passing vertically through the ceiling of the wind tunnel. This rod was held by a ball-bearing slide so that it was prevented from horizontal motion, but was free to move away from the wall. The rod was pulled upwards by a spring whose upper end was attached to a micrometer. Contact between the base of the model and the wall limited the upward motion of the model and provided a fixed position from which the extension of the spring could be measured. By adjusting the micrometer, the spring force acting on the

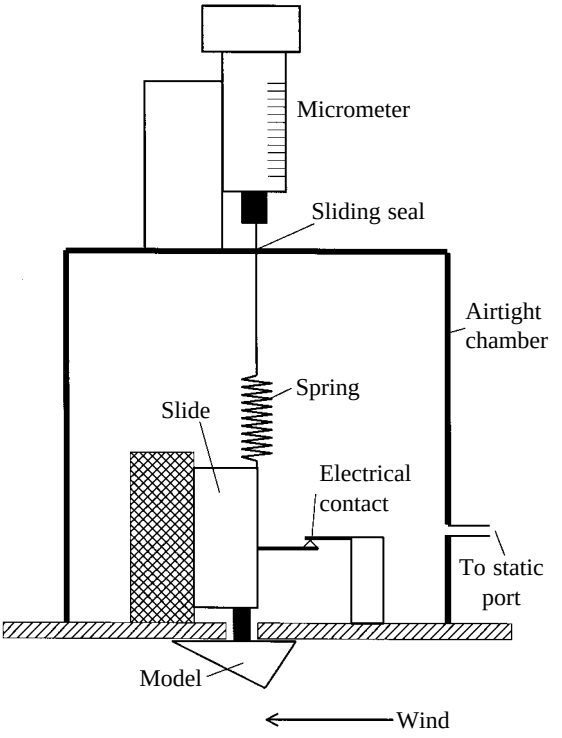

Fig. 6. A schematic diagram of the nulling force transducer used to measure lift on model limpets. Not drawn to scale. A length of flexible tubing (not shown) connected the air-tight housing to a static port in the wall of the wind tunnel, thereby equalizing the pressure in the housing with the pressure in the wind tunnel.

rod could be varied, and the position of the micrometer (accurately readable to within 0.1 mm) provided a measure of how far the spring had been stretched. The combined weight of the slide, rod and model was largely resisted by a counterweight, so the spring force applied to the rod was needed primarily to offset any lift force applied to the model. When the base of the model was firmly in contact with the wind tunnel's ceiling, an electrical contact was closed, causing a tone to be played into earphones worn by the experimenter. Any movement of the model away from the wall broke the contact and interrupted the tone, providing an unambiguous signal that the model had been displaced. To measure the lift on a model, the wind tunnel was turned on, the wind was allowed to stabilize at a specified speed, and the tension in the spring was gradually reduced to the point where the model was just displaced from the wall. The amount by which the spring was stretched at this point (read off of the micrometer) was a measure of the lift acting on the model. The apparatus was therefore used to null the force acting on the model and, thereby, provided a measure of lift when the model had not been displaced from the wall.

Lift and drag coefficients

The empirical measurements of lift and drag were used to calculate lift and drag coefficients. From equations 1 and 3:

$$C_{\mathrm{L}} = \frac{L}{p_{\mathrm{d}} A_{\mathrm{pl}}} , \tag{18}$$

$$C_{\mathrm{D}} = \frac{D}{p_{\mathrm{d}} A_{\mathrm{pr}}} . \tag{19}$$

Centers of lift and drag

The tendency of the distributed lift force to cause a model to rotate can be simulated if the overall lift is assumed to act along an axis running through the center of lift. Similarly, the rotational effects of distributed drag can be simulated by having the overall drag act along an axis running through the center of drag. These force centers are found through the following relationships. To locate the center of lift along the y axis (parallel to flow) in the plane of the wall, the torsional effect of each small component of lift is calculated as $y(i,j)\Delta L(i,j)$, where $y(i,j)$ is the distance from the origin at which the force component acts. Here, y=0 is located arbitrarily at the upstream edge of the model. The sum of these torsional effects across all areas of the model is the net torque acting about the x axis. This torque is then set equal to the product of the overall net lift acting on the model (L) and the (as yet unknown) distance from the origin at which this net lift would have to act to simulate the overall torque:

$$\sum_{\text{all } j} \sum_{\text{all } i} y(i,j)\Delta L(i,j) = y_{\mathrm{lc}} L , \tag{20}$$

where y_{lc} is the location on the y axis of the center of lift. Dividing both sides of the equation by L, we conclude that:

$$y_{\mathrm{lc}} = \frac{\sum_{\text{all } j} \sum_{\text{all } i} y(i,j)\Delta L(i,j)}{L} . \tag{21}$$

Similar equations describe the location of the center of lift along the x axis (perpendicular to flow):

$$x_{\mathrm{lc}} = \frac{\sum_{\text{all } j} \sum_{\text{all } i} x(i,j)\Delta L(i,j)}{L} , \tag{22}$$

and the location of the center of drag in the x,z plane:

$$z_{\mathrm{dc}} = \frac{\sum_{\text{all } j} \sum_{\text{all } i} z(i,j)\Delta D(i,j)}{D} , \tag{23}$$

and

$$x_{\mathrm{dc}} = \frac{\sum_{\text{all } j} \sum_{\text{all } i} x(i,j)\Delta D(i,j)}{D} . \tag{24}$$

Flow separation and turbulence

The distribution of flow-induced pressures over an object is strongly affected by the nature of flow in the object's boundary layer (Schlichting, 1977; Vogel, 1994). For example, the pressure drag on an object is largely determined by the size of the low-pressure wake downstream of the object, and the size of the wake in turn depends on where the flow separates from the object's surface. The farther downstream the separation point, the smaller the wake and the lower the drag. By affecting the pressure distribution, the location of the separation point can also affect the magnitude of lift and the location of the center of lift. To visualize the flow over the conical models, small tufts of thread were inserted into the pressure ports, and the ports were sealed at their bases. The model was then mounted in the wind tunnel as for the pressure distribution measurements and rotated through a series of angles. In the wind, the tufts aligned themselves with the local flow. In a laminar boundary layer, the tufts would lie still. Separation (and the accompanying boundary-layer turbulence) was evident as the tufts reoriented rapidly and unpredictably. Photographs of the tufts taken with a shutter speed of 1/30–1/60 s therefore provided a useful visual record of boundary-layer flow. Over those portions of the model with a laminar boundary layer, the tufts were clearly visible in the photographs and indicated the direction of local flow; over portions of the model with turbulent, separated flow, the tufts were evident in the photographs only as blurs.

Theory

Consider the object shown in Fig. 7A. A cone (a model for

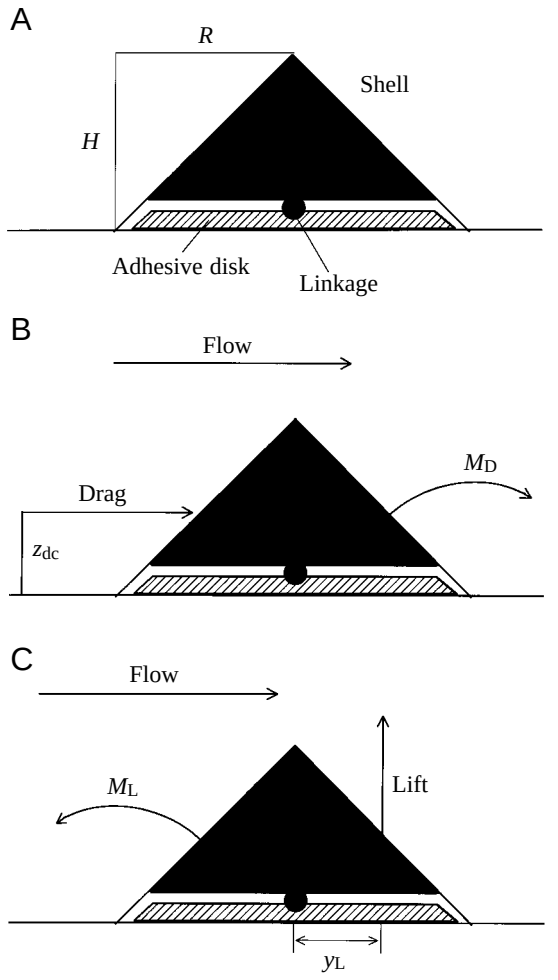

Fig. 7. Definition of terms used in the theoretical calculation of stresses acting on a limpet's basal adhesive. R, radius; H, height; z_{dc}, position of center of drag along the z axis; M_D, torque imposed by drag; M_L, torque imposed by lift; y_L, moment arm (y_{lc}–R), where y_{lc} is the position of the center of lift along the y axis. See text for explanation.

a limpet shell) has height H and radius R, and the ratio of height to radius is k:

$$k = \frac{H}{R} . \tag{25}$$

Beneath the cone is an adhesive disk with the same radius as the cone. The ventral face of the disk is glued to the substratum, and the dorsal face is attached to the center of the cone's base by an inextensible linkage. The adhesive disk and linkage are intended to model the foot of a limpet and its muscular suspension from the shell.

Flow past the cone imposes lift and drag forces that have a tendency both to cause the cone to slide downstream (a translation) and to cause it to overturn (a rotation). What forces must act on the adhesive disk if the cone is to remain stationary? That is, what forces must be applied through the linkage between disk and cone to maintain both translational and rotational equilibrium?

Drag acts in accordance with equation 3. In this case, $A_{pr}=kR^2$, so:

$$D = p_d k R^2 C_D . \tag{26}$$

This force has both translational and rotational effects. First, the tendency for drag to slide the shell downstream applies a shear to the glue beneath the disk, and the cone is in horizontal translational equilibrium when the magnitude of this shear force is equal to drag. This horizontal shear acting over the area of the disk results in a shear stress, τ:

$$\tau = \frac{D}{\pi R^2} . \tag{27}$$

Because this shear stress is imposed by drag, its magnitude depends on fluid velocity. To a first approximation, this dependence can be removed if we normalize the shear stress to the dynamic pressure of flow. The result is a dimensionless index of shear stress, τ':

$$\tau' = \frac{D}{\pi R^2 p_d} = \frac{k C_D}{\pi} . \tag{28}$$

Note that this normalization assumes that C_D is constant. In reality, the drag coefficient is a function of the Reynolds number, but measurements by Denny (1995) suggest that variation in C_D with Re is small over the range relevant to the present study.

Second, because the center of drag is at z_{dc}, above the base of the cone, drag acts to rotate the cone in a sense such that the upstream edge of the shell tends to be raised (Fig. 7B). This rotation (in a clockwise direction as viewed here) is arbitrarily defined as a negative rotation. The torque M_D imposed by drag has a magnitude equal to the product of drag D and the length of the moment arm perpendicular to the line of action of drag (z_{dc}):

$$M_D = -z_{dc} D . \tag{29}$$

Similarly, lift has both translational and rotational effects. The lift acting on the cone pulls up on the linkage (Fig. 7C), placing the basal adhesive in tension. The cone is in vertical translational equilibrium when the magnitude of this tensile force is equal to, or greater than, lift. (Any 'extra' force pulling down on the cone will be resisted by reaction forces acting through the cone's margins.)

As will be shown below, the center of lift of a symmetrical cone is typically located downstream of the center of adhesion (the center of the adhesive disk), and thus lift acts to rotate the cone in a positive direction (Fig. 7C). In this case, the torque, M_L, is the product of the net lift, L, and the moment arm, $y_L=y_{lc}-R$:

$$M_L = y_L L . \tag{30}$$

For example, if the center of lift is at the center of the planform area (directly above the adhesive linkage), $y_{lc}=R$, and no moment is present.

The horizontal and vertical translational effects of drag and lift (respectively) do not interact, but the applied torques do. As a result, the net torque M acting on the cone is the sum of the (usually counteracting) moments from drag and lift:

$$M = M_D + M_L . \quad (31)$$

For the shell to be in rotational equilibrium, this net moment must be resisted by a counteracting moment provided by the vertical component of tension in the linkage between the disk and the cone acting relative to an axis of rotation either at the upstream edge of the shell (if M is positive) or at the downstream edge of the shell (if M is negative). Because the linkage has a moment arm of R relative to either the upstream or downstream edge of the shell, the required tensile force is:

$$T = \frac{M}{R} . \quad (32)$$

Depending on the magnitude of M, T may be different from L. T_{act}, the actual vertical component of tension in the linkage, will be the greater of these two forces. As noted above, if T exceeds L, the additional vertical force required for vertical translational equilibrium is provided by reaction forces at the shell's margin.

The imposition of T_{act} imposes a tensile stress on the basal adhesive:

$$\sigma = \frac{T_{act}}{\pi R^2} . \quad (33)$$

As with drag, this stress can be normalized to the dynamic pressure of the flow:

$$\sigma' = \frac{\sigma}{p_d} = \frac{T_{act}}{\pi R^2 p_d} . \quad (34)$$

Note that this normalization assumes that C_L is constant. Measurements made by Denny (1995) suggest that C_L for limpets decreases with increasing velocity, but only slightly (on average C_L is proportional to $u^{-0.027}$).

The stresses placed on the basal adhesive are an index of the risk that the limpet will be dislodged. It is often useful to compare this risk with the benefit accruing to the limpet if it stays attached. Here, I assume that the biological benefit of attachment is proportional to the body volume of the limpet. For example, the larger the volume beneath the shell, the larger the gonad the limpet can produce and the larger its potential reproductive output. Other indices of benefit could be chosen to address specific aspects of limpet biology, but this simple index is appropriate for the general nature of the present discussion. The volume of a cone is $\frac{1}{3}\pi R^2 H$. In terms of the height-to-radius ratio k, volume is $\frac{1}{3}\pi R^3 k$. For present purposes, it will be useful to express this volume relative to a standard volume – the volume of a cone with radius R and a height-to-radius ratio of 1. Thus, the dimensionless normalized volume of a cone is simply k.

This normalized volume can then be used to calculate two dimensionless indices of risk per benefit:

$$B_{shear} = \frac{\tau'}{k} , \quad (35)$$

$$B_{tension} = \frac{\sigma'}{k} . \quad (36)$$

Results

Symmetrical cones

The average pressure measured directly beneath a cone (open circles, Fig. 8) is closely approximated by the average pressure measured at ports around the cone's rim (filled circles). The higher spired the cone, the greater the tendency for flow to go around the base rather than over the top. As a result, the higher the spire, the faster the basal flow and, therefore (in accordance with Bernoulli's principle), the basal pressure becomes increasingly negative as the height-to-radius ratio of the cone increases. p_b varies between −5 % and −30 % of the dynamic pressure. In his measurements of lift on limpets, Denny (1989, 1995) mistakenly assumed that the pressure beneath the organism was equal to ambient static pressure in the surrounding flow and, as a result, these measurements are

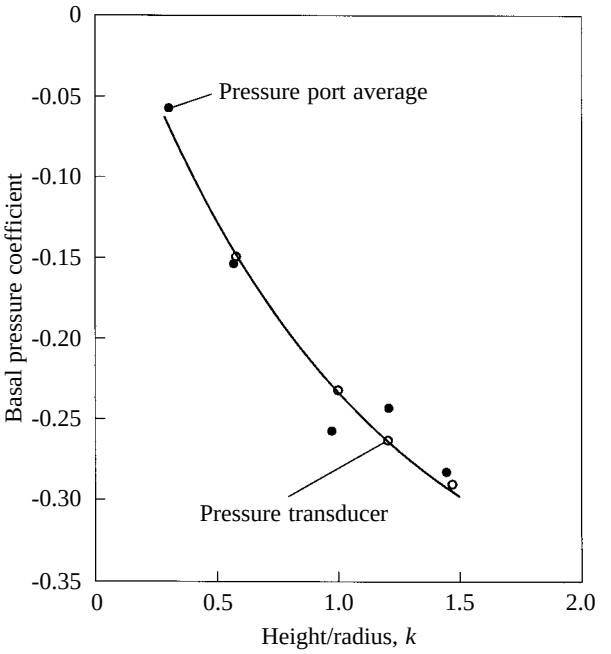

Fig. 8. The basal pressure coefficient (pressure/dynamic pressure) for a cone in flow *versus* the height-to-radius ratio (k) of the cone. The solid line is a least-squares fit to the data: pressure coefficient=$-0.397+0.444e^{-k}$ (r^2=0.971, P<0.001). This equation should be used only for the range of k encountered in these experiments (0.30–1.45). Open circles, pressures measured using the pressure transducer; filled circles, pressures measured at points around the cone's rim.

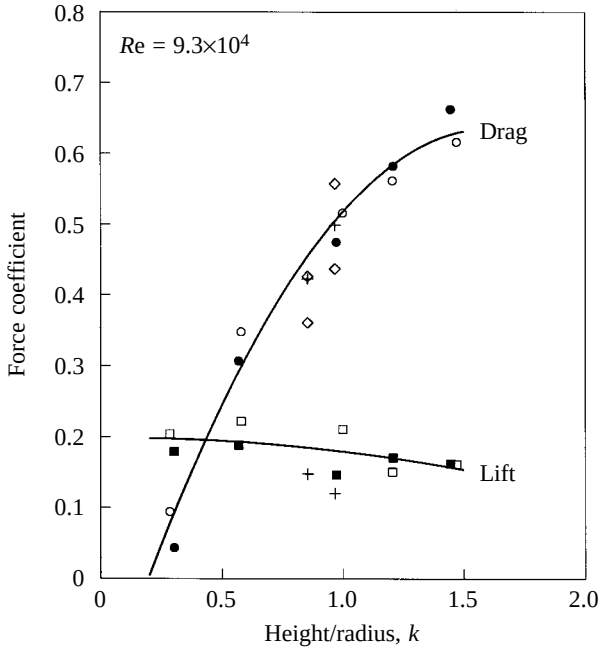

Fig. 9. The variation in lift and drag coefficients for cones as a function of their height-to-radius ratio (*k*); open circles, direct measurements of drag; filled circles, drag calculated from pressure distributions; open squares, direct measurements of lift; filled squares, lift calculated from pressure distributions; diamonds, drag for asymmetrical cones with their apices upstream and downstream; plus signs, drag and lift for asymmetrical cones broadside to the flow. *Re*, Reynolds number. Equations for the least-squares regression lines are given in the text.

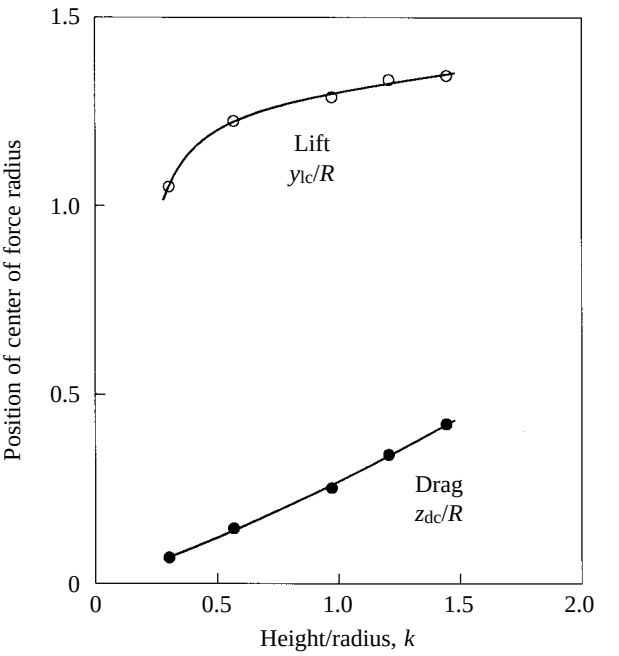

Fig. 10. The variation in location of the centers of lift (y_{lc}) and drag (z_{dc}) as a function of the height-to-radius ratio (*k*). In each case, the parameter has been normalized to the cone's radius, *R*. Equations for the least-squares regression lines are given in the text.

likely to be overestimates by 5–30 %, depending on the 'peakedness' of the shell.

The drag coefficients estimated through a calculation of the pressure distribution over cones (filled circles, Fig. 9) closely match those estimated through direct measurement of drag (open circles). The drag coefficient rises dramatically with an increasing ratio of height to radius. For use in the estimation of stresses, this variation is modeled using the following equation (the drag curve in Fig. 9):

$$C_D = 0.394 + 0.223k - \frac{0.114}{k}\,, \qquad (37)$$

an expression that accounts for 98.6 % of the variation in C_D ($P<0.001$).

Lift forces estimated from pressure distributions and direct measurement generally agree [the average fractional difference is 10.4 %, with the direct measurement (open squares) providing the higher value in three out of five instances, see Fig. 9]. The lift coefficient is relatively constant across ratios of height to radius, decreasing only slightly with an increase in *k*. For use in the estimation of stress, C_L is modeled as follows (the lift curve in Fig. 9):

$$C_L = 0.198 + 0.004k - 0.022k^2\,. \qquad (38)$$

This expression accounts for only 36.6 % of the variation in C_L ($P<0.05$), but note that the magnitude of variation here is small.

The locations of the centers of lift and drag in symmetrical cones are shown in Fig. 10. The center of lift (measured as the distance from the upstream edge of the shell) is always downstream of the cone's apex ($y_{lc}/R>1$), and as the cone becomes more highly spired, the center of lift moves farther downstream (y_{lc}/R increases). The center of drag (measured from the plane of the cone's base) moves farther away from the substratum the more high-spired the cone. These relationships are modeled by the following equations (the curves in Fig. 10):

$$\frac{y_{lc}}{R} = 1.235 + 0.085k - \frac{0.019}{k^2}\,, \qquad (39)$$

$$\frac{z_{dc}}{R} = 0.216k + 0.053k^2\,, \qquad (40)$$

and account for 99.6 % ($P<0.001$) and 93.0 % ($P<0.002$) of the variation in the location of the lift and drag centers, respectively. Note that equations 37–40 apply only to the range of *k* used in these experiments (0.302–1.445) and should not be used to estimate values beyond this range.

The dimensionless stresses placed on symmetrical cones are shown by the curves in Fig. 11 (the individual symbols refer to asymmetrical cones and will be discussed below). The shear stress (due to drag alone) increases monotonically with increasing *k*, while the tensile stress decreases monotonically

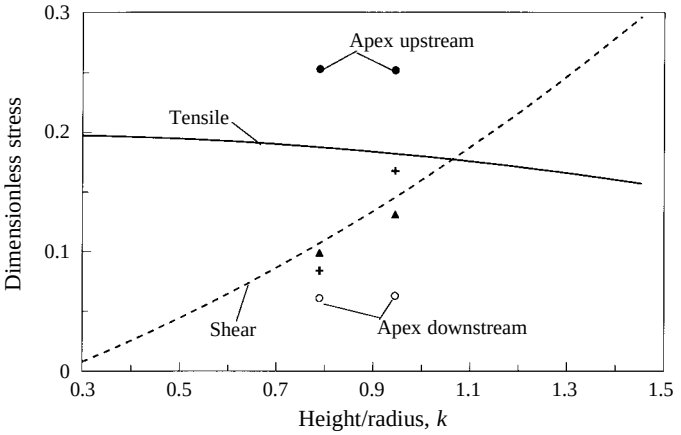

Fig. 11. The variation in dimensionless stress (stress per dynamic pressure) placed on a limpet's basal adhesive as a function of the height-to-radius ratio *k*. The curves represent data for symmetrical cones, and the individual symbols represent data for asymmetrical cones. Filled circles denote tensile stress for an orientation with the apex upstream, open circles are for the apex downstream. The plus signs and triangles denote shear stresses with the apex downstream and upstream, respectively.

with increasing *k*. Tensile stress is greater than shear stress for $k<1.06$.

The pressure distributions for symmetrical cones of various height-to-radius ratios are shown in Fig. 12. A zone of high pressure is present on the lower elevations of the upstream face, gradually giving way to low pressures lateral to the apex and at the higher upstream elevations. Pressure is low on the downstream face of the cone, and spatial variation in pressure is much less pronounced. The prime exception to these generalities is found in the lowest-spired cone (Fig. 12C, $k=0.30$), for which the pressure distribution is very nearly symmetrical between the upstream and downstream faces. This symmetry is consistent with the low drag coefficient measured for this cone (Fig. 9).

The location of flow separation over symmetrical cones (as revealed by the tufts of thread) is shown in Fig. 13. There is a pronounced flow separation on the downstream shoulders of a typical model, and some reverse flow is usually evident on the downstream face. The angle of separation is the same at all heights on the cone (within the 10° resolution of the method used here) and moves aft as the height-to-radius ratio decreases. For the lowest-spired cone, separation occurs in a narrow swath directly downstream of the apex. This is indicative of a small wake and supports the measurements noted above of a low drag coefficient for this model.

The components of the risk–benefit index for symmetrical cones are shown in Fig. 14. The risk from tension decreases monotonically with increasing peakedness, and the risk from shear increases monotonically with increasing *k*. The two risks cross at $k=1.06$. Note that the actual risk is the greater of these two; they do not add. As a result, these calculations suggest that conical limpets could minimize the risk of enclosing a body of a given volume by producing a shell with a height-to-radius ratio of 1.06. Several assumptions affect this conclusion, however, and these are addressed in the Discussion.

Asymmetrical cones

The drag coefficients of asymmetrical cones with their apices either upstream or downstream (open diamonds, Fig. 9) are close to those measured for symmetrical cones of similar height-to-radius ratio. For the less asymmetrical cone (Fig. 2A) oriented with its apex upstream, the drag coefficient is slightly higher than for a comparable symmetrical cone and slightly lower when the apex is downstream. Drag on the more asymmetrical cone (Fig. 2B) is slightly lower than that expected for a comparable symmetrical cone, regardless of the upstream or downstream orientation of the apex. Recall that, for these asymmetrical cones, 'peakedness' is measured as the ratio of height to half the length in the direction of flow.

The lift coefficients of asymmetrical cones (filled circles, Fig. 15) differ substantially from those of cones with a central apex (open circles). When the apex is upstream of the center of the planform ($E<1$), the lift coefficient of the asymmetrical cones is approximately five-thirds that on symmetrical cones, and when the apex is downstream ($E>1$) the lift coefficient is approximately half that on symmetrical cones.

The pressure distribution over asymmetrical cones is qualitatively similar to that over symmetrical cones (Fig. 16), but the relative areas subjected to high and low pressures are changed as a result of the shift in the position of the apex. When the apex is upstream (Fig. 16A,B), high pressures are confined to the steep upstream slope of the cone, while low pressure acts over the broad leeward slope. The net result is the relatively large lift noted above. In contrast, when the apex is downstream (Fig. 16C,D), high pressures act over the broad upstream slope while the lowest pressures are confined to the steep leeward slope, and lift is small.

When the asymmetrical cones are orientated broadside to the flow, the distribution of pressure is no longer bilaterally symmetrical (Fig. 17) and is intermediate between that seen in upstream and downstream orientations. Less of the cone's area is downstream of the apex (where pressures are lowest) than when the apex is upstream, and the lift coefficient is therefore reduced. However, when the cone is orientated broadside to the flow, more of its area is downstream of the apex than when the apex is itself downstream, and the lift coefficient is consequently higher than that for a downstream orientation. The lift coefficients for these asymmetrical cones broadside to flow are slightly lower than for comparable symmetrical cones (crosses, Fig. 9).

The location of the center of lift, *CP*, varies with orientation for the asymmetrical cones (see Figs 16 and17). Note that, for the more asymmetrical cone orientated with its apex upstream (Fig. 16B), the center of lift lies upstream of the cone's center of planform area. As a consequence, in this case, the moment due to lift acts in the same direction as that due to drag, tending to raise the upstream edge of the shell. For the more asymmetrical cone with its apex downstream, the center of lift

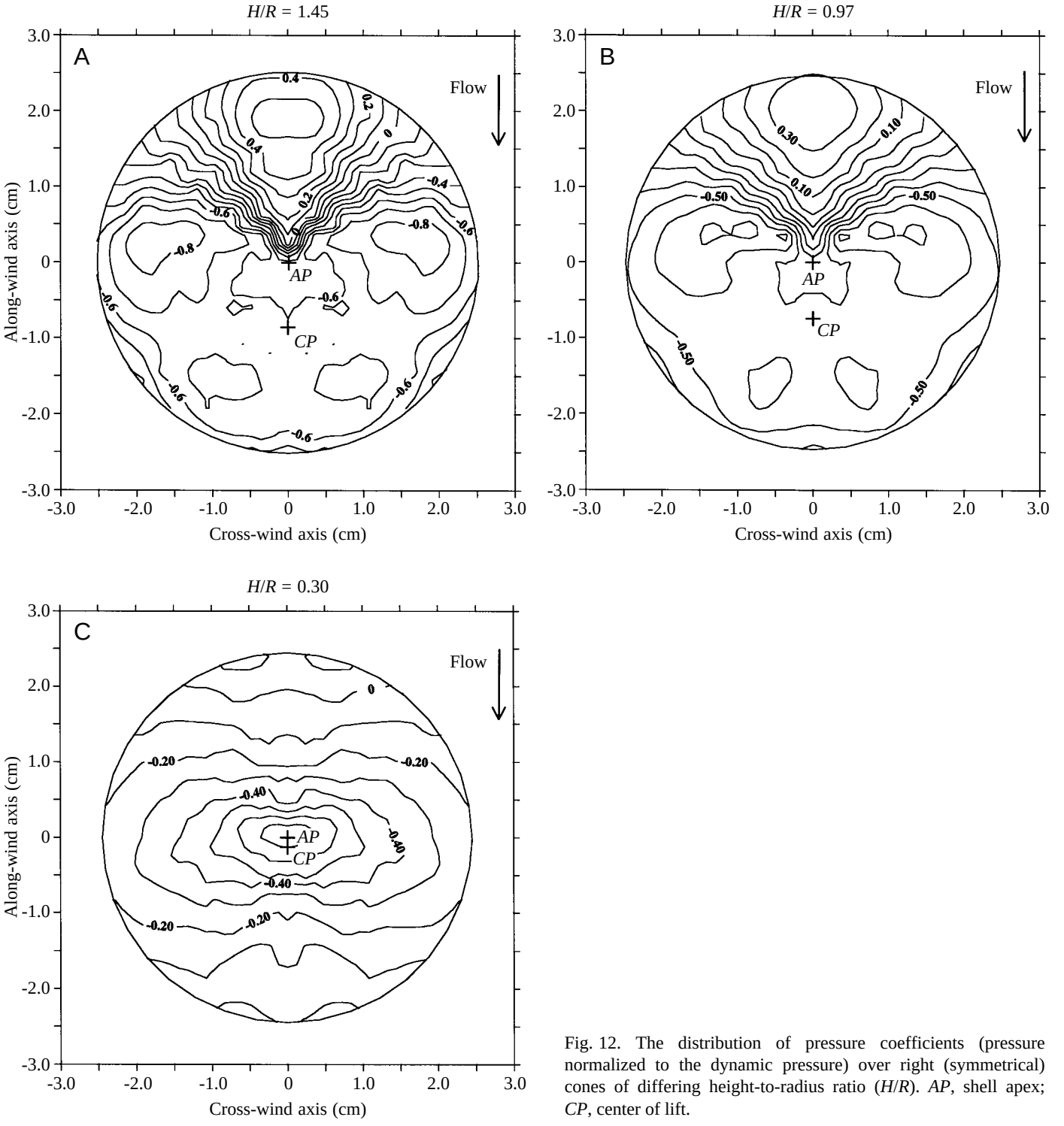

Fig. 12. The distribution of pressure coefficients (pressure normalized to the dynamic pressure) over right (symmetrical) cones of differing height-to-radius ratio (*H*/*R*). *AP*, shell apex; *CP*, center of lift.

is upstream of the shell's apex (although downstream of the center of the shell, Fig. 16D).

The flow-induced stresses in the basal adhesive of asymmetrical cones are shown by the circles in Fig. 11. When the apex of the cone is upstream, the resulting high lift coefficient results in a tensile stress larger than that for symmetrical cones of the same height-to-radius ratio (filled circles, Fig. 11). The opposite is true when the apex is orientated downstream (open circles, Fig. 11). Because of the similarity in drag coefficients for symmetrical and asymmetrical cones, the shear stress for the asymmetrical cones is similar to that for the symmetrical cones (plus signs and triangles, Fig. 11).

The lateral lift coefficient for the slightly asymmetrical cone was 0.087, and that for the very asymmetrical cone was 0.077. Both these values are small compared with the drag

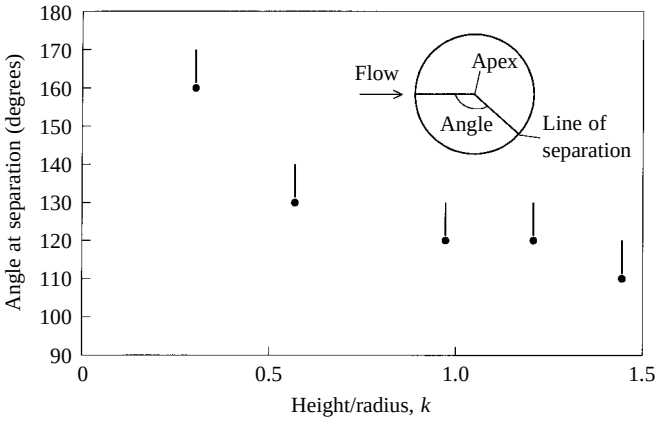

Fig. 13. The location of the line of flow separation for symmetrical cones as a function of the height-to-radius ratio *k*, estimated from photographs of tufts in flow. The filled circles denote the minimum angle at which separation occurs, the vertical lines the range in angle among ports at different heights on the shell.

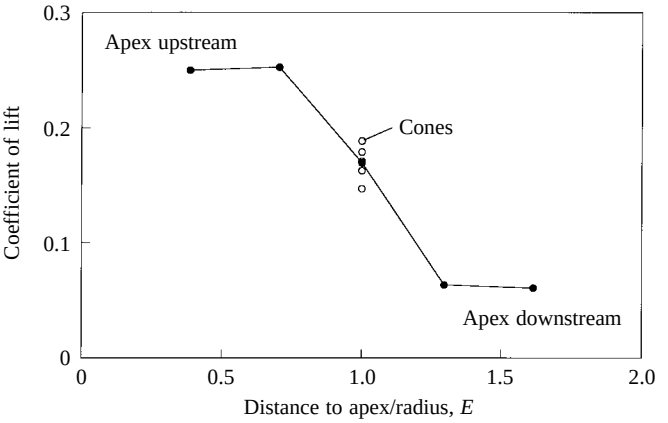

Fig. 15. Lift coefficient as a function of the location *E* of the apex in model limpets. Open circles are for symmetrical cones. The filled circle at *E*=1 (see equation 6) is the average of all measurements for centrally located apices; other filled circles are data for asymmetrical cones with the apex either upstream or downstream.

coefficients at this orientation (0.499 and 0.422, respectively) and may be due to the slight bilateral asymmetry in the placement of the pressure ports or to a slight misalignment of the shell's axis relative to the oncoming wind.

Discussion

The experiments reported here support four primary conclusions regarding the effect of limpet shell shape on hydrodynamic forces: (i) at a low ratio of height to radius, lift is the dominant force; (ii) at a high ratio of height to radius, drag is the dominant force; (iii) for symmetrical cones, the ratio of risk to nominal benefit has a minimum at a height-to-radius ratio of 1.06; (iv) displacement of the apex away from the center of the shell substantially increases tensile stress and overall risk when the apex is orientated upstream.

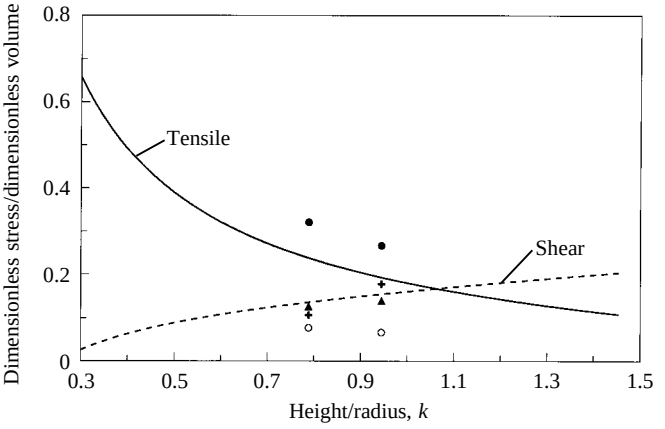

Fig. 14. The ratio of 'risk' (dimensionless stress) to 'benefit' (dimensionless volume) as a function of the height-to-radius ratio *k*. Lines are for symmetrical cones, individual symbols are for asymmetrical cones. Filled circles denote tensile risk for an orientation with the apex upstream, open circles are for the apex downstream. The plus signs and triangles denote shear risks with the apex downstream and upstream, respectively.

Given these conclusions, several questions arise. First, if the ratio of mechanical risk per body volume has been the sole guiding factor in the evolution of limpet shell shape, the third conclusion would lead one to predict that limpets would have a height-to-radius ratio near 1.06. Is this true? In reality, the vast majority of limpets are not so peaked. For 79 species of intertidal limpets selected haphazardly from the faunas of the Caribbean, New Zealand, Australia, Chile, Europe, Japan, South Africa and the west coast of North America (Table 2), the ratio of height to half length (analogous to height/radius) ranges from 0.34 to 1.27, with a mean of only 0.68±0.20 (mean ± S.D.), a median of 0.69 and a mode of approximately 0.73. For the same species, the ratio of height to half-width ranges from 0.41 to 1.57, with a mean of 0.85±0.25 (mean ± S.D.), a median of 0.81 and a mode of approximately 0.83. Although these data do not represent a thorough sampling of the world's wave-swept limpets, it is clear that limpets do not typically have shells as high-spired as the simple analysis proposed here would suggest is optimal (1.06).

There are several potential reasons for this disparity. First, the calculation of the risk–benefit ratio used here tacitly assumes that a given stress applied in tension incurs the same risk of dislodgment as stress applied in shear. This may not be the case. For example, in the most thorough study to date of the dependence of limpet adhesion on the angle of the applied force, Grenon and Walker (1981) found that *Patella vulgata* was substantially weaker in shear than in tension. The mean breaking stress in shear was 0.049±0.05 MPa, while the mean breaking stress in tension was 3.3 times greater, 0.162±0.121 MPa (means ± S.D.). Thus, if we assume that risk is linearly proportional to stress (for stresses near the mean), a given force applied in shear would incur 3.3 times the risk of a force applied in tension. This effect can be simulated in the present analysis by multiplying the index of risk in shear by a

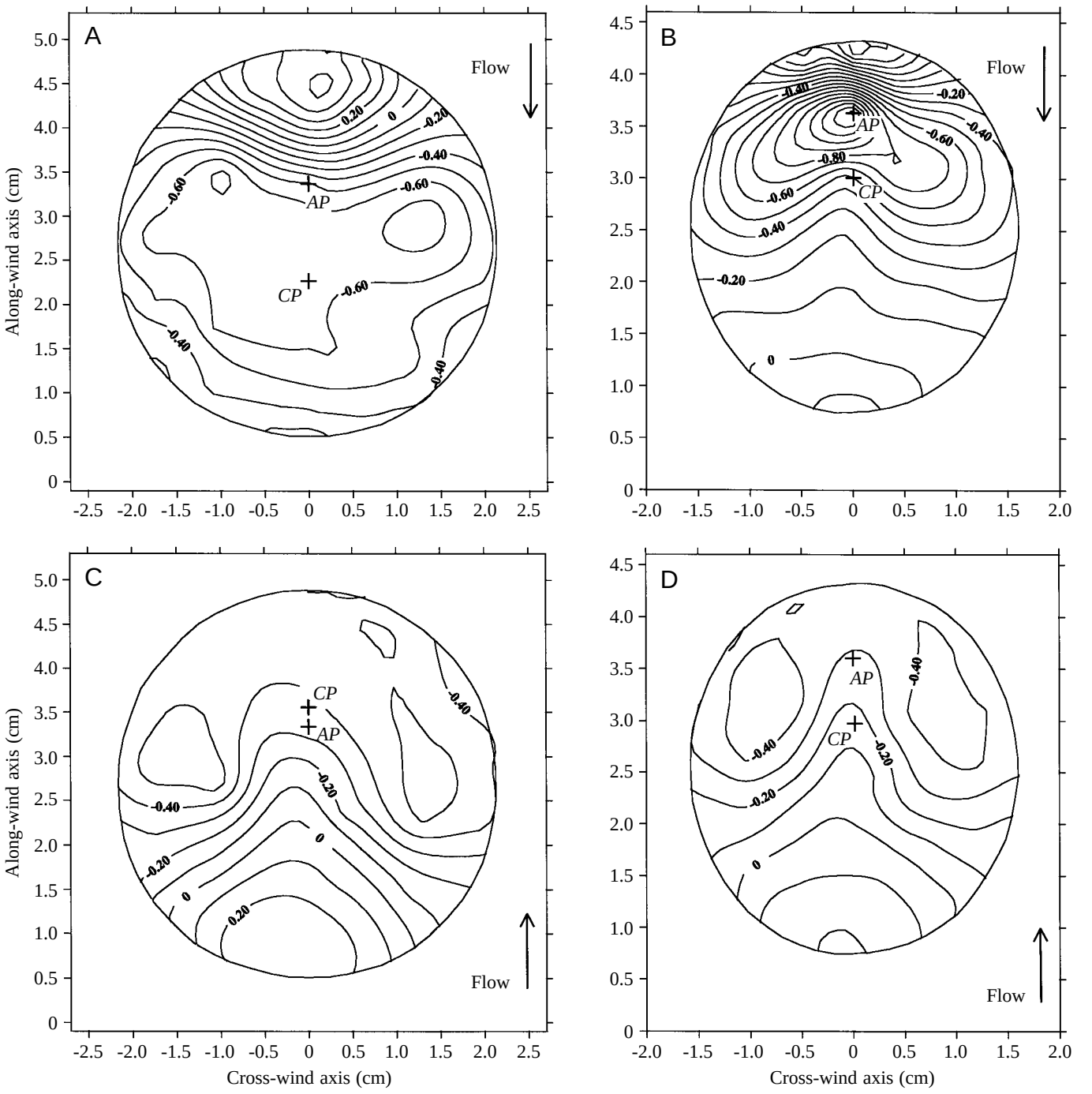

Fig. 16. The distribution of pressure coefficients (pressure/dynamic pressure) over asymmetrical cones. (A,C) The less asymmetrical cone; (B,D) the more asymmetrical cone. In A and B, the apex of the cone is upstream; in C and D, the apex is downstream. *AP*, apex; *CP*, center of lift.

factor of 3.3, as shown in Fig. 18. This increase of risk in shear is such that shear overtakes tension as the primary source of risk at a height-to-radius ratio of 0.57, close to the mean observed in nature (0.68), suggesting that limpets may indeed be optimally designed.

This explanation is unlikely to be operative in nature, however. The disparity between strengths in shear and tension reported by Grenon and Walker (1981) was measured for limpets attached to smooth Perspex. When shear strength was measured on slate, shear strength was indistinguishable from tensile strength. Furthermore, measurements on rugose rocks for *Lottia pelta* (Denny, 1989) and *Lottia gigantea* (Denny and Blanchette, 2000) showed that, under these conditions, shear strength was greater than tensile strength. Thus, when placed on a surface that provides the shell with some frictional resistance to shear, limpets are at least as capable of resisting forces in shear as they are of resisting tensile forces, and the optimal height-to-radius ratio should be 1.06 or greater.

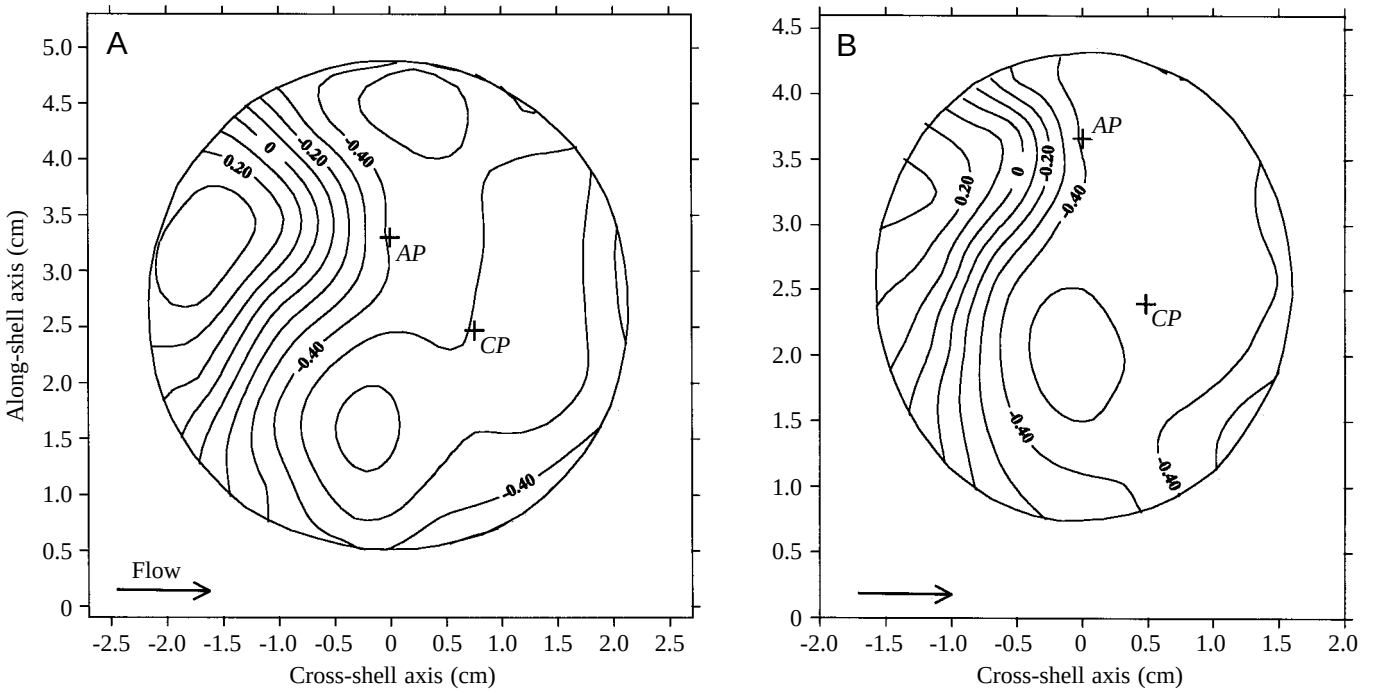

Fig. 17. The distribution of pressure coefficients (pressure/dynamic pressure) over asymmetrical cones oriented broadside to the flow. (A) The less asymmetrical cone; (B) the more asymmetrical cone. Flow is from the left. *AP*, apex; *CP*, center of lift.

Gaylord (1997, 2000) reports direct measurements of drag forces on organisms in the surf zone, and these data suggest that, for organisms initially out of the water, the force may be larger than expected from drag alone during the initial contact with an advancing wave front. This 'impingement force' can be modeled using the standard equation for drag, but with a drag coefficient that is (for rigid objects such as limpet shells) multiplied by an average factor of 1.3. In exceptional cases, this factor may be as high as 3. If these large impingement forces indeed apply to limpets in the surf zone, drag forces will be larger than calculated here, leading to an increase in shear stress. The resulting scenario is presented in Fig. 18. If impingement acts to increase drag by the average amount measured by Gaylord (1997), the optimal value of k for symmetrical cones is approximately 0.92, still in excess of the average among extant limpets. If drag is increased by a factor of 3, the optimal height to radius ratio is approximately 0.60, tantalizingly close to the average height-to-half-length ratios for extant limpets (0.68). There is considerable uncertainty regarding this calculation, however. First, Fig. 18 has been produced by increasing drag while holding lift constant. Because both lift and drag are functions of the pressure distribution over limpets, it seems very likely that impingement-flow effects that lead to an increase in drag will also increase lift. If this is the case, the optimum shape implied by Fig. 18 is illusory. Unfortunately, Gaylord (1997, 2000) did not measure lift, so resolution of the potential for impingement effects to select for shell shape awaits further data.

The fourth conclusion above suggests that risk is minimized if the shell's apex is located centrally. Just as limpet shells seem not to have the optimal height-to-radius ratio expected on the basis of hydrodynamic forces, they also seem not to have an optimal placement of the shell apex. For the sampling of limpet species shown in Table 2, the apex of the shell is typically displaced anterior of the shell's center by approximately 15 % of the shell's length (E=0.71). This

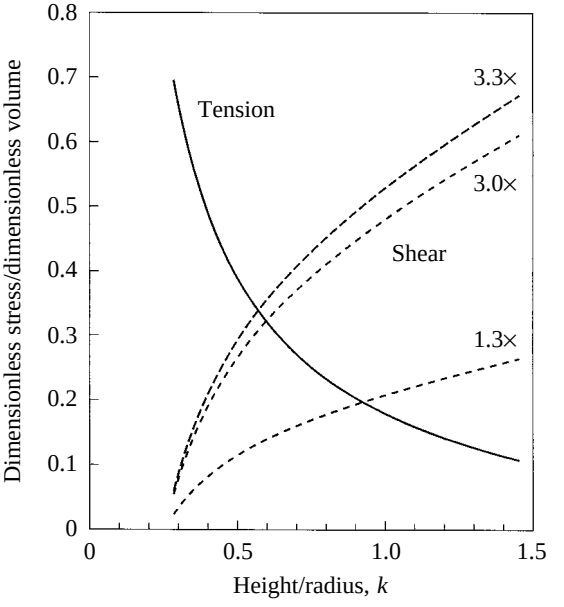

Fig. 18. Variation in the 'risk–benefit' ratio as a function of the height-to-radius ratio k. Here, the risk of dislodgment in shear has been multiplied to reflect the possible relative weakness of limpets in resisting shearing forces or the increase in drag due to impingement effects. Note that the implied shifts in the optimal height-to-radius ratio are unlikely to apply in nature (see text).

Table 2. *Morphological attributes of limpets*

Origin		$\frac{H}{\lambda/2}$	$\frac{H}{W/2}$	E	Origin		$\frac{H}{\lambda/2}$	$\frac{H}{W/2}$	E
California	*Acmaea mitra*	1.274	1.394	0.892	Australia	*Patelloida latistrigata*	0.692	0.920	
	Lottia conus	0.463	0.594	0.766		*Patelloida mimula*	0.768	1.026	0.780
	Lottia digitalis	0.728	0.885	0.534		*Patelloida mufria*	0.922	1.394	0.702
	Lottia gigantea	0.495	0.641	0.648		*Patelloida nigrosulcata*	0.900	1.150	
	Lottia limatula	0.531	0.596	0.626		*Patelloida profunda*	0.784	1.092	0.758
	Lottia pelta	0.810	1.003	0.792		*Patelloida saccharina*	0.620	0.764	0.784
	Lottia strigatella	0.736	0.904	0.624		*Patelloida victoriana*	0.730	0.928	0.640
	Lottia ochracea	0.669	0.907	0.532	Europe	*Patella caerulea*	0.702	0.842	0.642
	Macclintockia scabra	0.595	0.656	0.694		*Patella rustica*	0.720	0.908	0.760
	Tectura scutum	0.455	0.575	0.678		*Patella vulgata*	0.750	0.876	0.916
	Tectura persona	0.816	1.000	0.758					
	Tectura fenestrata	0.681	0.798	0.758	Japan	*Notoacmea schrenkii*	0.388	0.526	0.778
South Africa	*Patella argenvillei*	0.946	1.292	0.844		*Notoacmea gloriosa*	0.410	0.512	0.598
	Patella barbara	0.848	1.100	0.858		*Notoacmea boninensis*	0.396	0.486	0.610
	Patella concolor	0.428	0.526	0.718		*Notoacmea concinna*	0.524	0.618	0.788
	Patella granatina	0.696	0.768	0.916		*Notoacmea fuscoviridis*	0.486	0.614	0.692
	Patella granularis	0.780	1.000	0.622		*Notoacmea radula*	0.456	0.534	0.616
	Patella longicosta	0.480	0.522	0.676		*Notoacmea nigrans*	0.594	0.750	0.600
	Patella miniata	0.446	0.546			*Notoacmea teramachii*	0.538	0.652	0.766
	Patella hoffmani	0.648	0.780	0.588	Caribbean	*Acmaea albicosta*	0.474	0.648	0.794
	Patella cochlear	0.476	0.698	0.814		*Acmaea cubensis*	1.092	1.346	0.726
	Patella ocularis	0.452	0.518	0.738		*Acmaea pustulata*	0.722	0.974	0.904
	Cellana capensis	0.562	0.728	0.686		*Collisella leucophora*	1.068	1.314	0.496
	Helcion petunculus	0.762	0.962	0.976		*Lottia balanoides*	0.964	1.252	0.720
Australia	*Patellanax chapmani*	0.586	0.764	0.820		*Lottia tranquebenca*	0.580	0.772	0.556
	Patellanax peroni	0.708	0.836	0.784		*Tectura candeana*	0.506	0.642	0.778
	Patellanax laticosta	0.992	1.290	0.710		*Tectura elegans*	0.464	0.572	0.700
	Cellana solida	0.834	1.014	0.726		*Tectura tenara*	0.602	0.800	0.714
	Cellana tramoserica	0.948	1.198	0.748	Chile	*Collisella boehimita*	0.336	0.408	0.664
	Cellana conciliata	0.654	0.796	0.748		*Collisella orbingyi*	0.526	0.656	0.594
	Cellana turbator	0.736	0.984	0.762		*Scurria araucana*	0.586	0.690	0.520
	Notoacmea alta	1.256	1.570	0.650		*Scurria ceciliana*	0.722	0.858	0.448
	Notoacmea corrodea	0.688	0.870	0.644		*Scurria parasitica*	0.532	0.682	0.634
	Notoacmea flammea	0.734	0.878	0.534		*Scurria scurra*	1.226	1.364	0.716
	Notoacmea mayi	0.512	0.644	0.780		*Scurria variabilis*	0.446	0.554	0.608
	Notoacmea petterdi	0.706	0.808	0.482		*Scurria viridula*	0.562	0.660	0.680
	Collisella mixta	0.902	1.016	0.676		*Scurria zebrina*	0.742	0.914	0.722
	Collisella onychitis	0.704	0.812	0.754		Mean	0.682	0.849	0.702
	Patelloida alticosta	0.694	0.800	0.756		S.D.	0.203	0.254	0.108
	Patelloida bellatula	0.682	0.934			Median	0.688	0.808	0.710
	Patelloida cryptalirata	0.562	0.722	0.490		Mode	≈0.725	≈0.825	≈0.775
	Patelloida. heteromorpha	0.760	0.908	0.694					
	Patelloida insignis	0.944	1.164	0.676					

Note that the apex as used here is the highest point on the shell; it may deviate from the anatomical apex. Data are from MacPherson (1955), Ponder and Creese (1980), Lindberg (1981) and Denny (1995), and measurements were made on shells at the Museum of Paleontology, University of California, Berkeley, USA.

H, height; λ, length; *W*, width; *E*, proportional location of shell apex (see equation 6).

displacement typically incurs an increase in lift on the shell when the apex is upstream and a decrease when the apex is downstream (Denny, 1995). If limpets were able to predict the direction from which maximal flow arrived, they could orient themselves appropriately to minimize the lift imposed. Unfortunately, flow is often sufficiently chaotic in the surf zone of wave-swept shores that prediction of the direction of maximal velocity is unlikely; Denny (1985) reported that, in a typical intertidal habitat, the direction of maximal velocity measured at a fully exposed site was indistinguishable from random. As a result, during its lifetime, a limpet is likely to encounter large fluid velocities from all directions, and the

increased lift associated with those velocities arriving from the anterior increases the overall risk of dislodgment. These considerations again lead to the conclusion that limpet shells are not optimally designed to resist hydrodynamic forces.

When viewed from a different perspective, this conclusion does not seem surprising. Fig. 11 shows that, for the range of shell shapes found in extant limpets, the dimensionless stress for a symmetrical cone varies between 0.177 at the optimum height-to-radius ratio and 0.296 for a very high-spired shell. What water velocities are required to impose these dimensionless stresses on a limpet with a given adhesive strength? If we assume that C_D and C_L are constant and recall that $p_d=\frac{1}{2}\rho u^2$, we can set the applied tensile stress σ equal to the breaking stress σ_b in equation 33 and solve equation 34 for velocity:

$$u = \sqrt{\frac{2\sigma_b}{\rho\sigma'}} \, . \qquad (41)$$

Here, σ' is either 0.177 or 0.296. The results are shown as the solid curves in Fig. 19.

The upper limit of this graph is set at the highest water velocity ever recorded on shores (25 m s^{-1}, M. W. Denny, unpublished data). Given this approximate limit to the imposed water velocity, it is apparent that, if the adhesive strength of a conical limpet exceeds approximately 0.1 MPa, a typical limpet will not be dislodged regardless of its shape. An average limpet has a mean tenacity of 0.28±0.14 MPa (mean ± S.D., N=10) (data from Branch and Marsh, 1978; Grenon and Walker, 1981; Denny, 1989; M. W. Denny, unpublished data), and strengths as high as 0.69 MPa have been measured. In other words, given the adhesive strength of most limpets, the less-than-optimal shape of the shell is unlikely to result in any substantial increase in mortality.

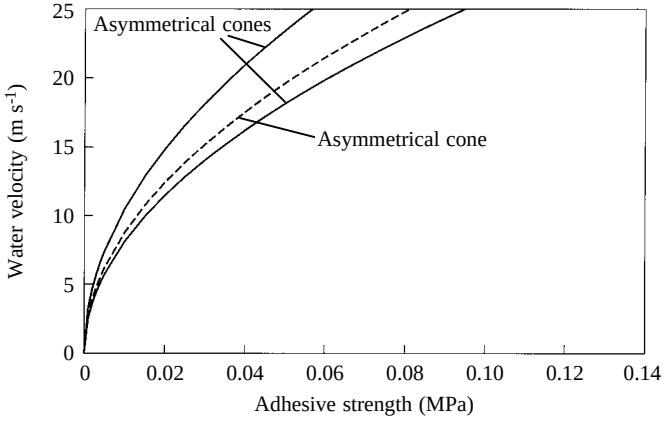

Fig. 19. The water velocity required to dislodge limpets of a given adhesive tenacity. Solid lines, symmetrical cones. The lower solid curve represents a low-spired shell with a dimensionless stress of 0.296. The upper solid curve represents an optimally spired shell with a dimensionless stress of 0.177. Dashed line, the more asymmetrical experimental cone oriented in its most vulnerable posture (apex upstream).

Even for limpets that have exceptionally low tenacities, shell shape may be of limited importance in selection. For example, consider a limpet such as *Lottia pelta* or *Lottia gigantea* with a stationary tenacity of 0.12 MPa (Denny, 1989; Denny and Blanchette, 2000). The results of Miller (1974) suggest that, when these limpets move to forage, their tenacity may be as low as 0.04 MPa. At this low tenacity, water velocities commonly found on wave-swept shores are capable of dislodging these animals (Fig. 19). The range of critical velocities is narrow, however. At an adhesive tenacity of 0.04 MPa, a water velocity in excess of 20.9 m s^{-1} will dislodge a conical limpet regardless of its shape, while a velocity less than 16.2 m s^{-1} will not dislodge the limpet, again regardless of shape. In other words, even when shape potentially makes a difference in the survivorship of limpets, hydrodynamic forces can act as a selective factor only if the maximal water velocity encountered by a limpet falls within a narrow range, a range only 4.7 m s^{-1} wide in this example. Anterior displacement of the shell's apex (dashed line, Fig. 19) results in a tenacity/velocity curve similar to that of a high-spired symmetrical cone: once again, shape matters only if the adhesive tenacity of the limpet is quite low.

In the light of these analyses, one conclusion seems clear: the evolved shape of limpet shells (presumably guided by the selection pressure due to flow-induced mortality) is 'good enough' to keep applied hydrodynamic forces within the bounds set by the animals' adhesive system, but flow-induced mortality has not been sufficient to optimize the shells' lift and drag coefficients. It is perhaps surprising that limpets, living in one of the most extreme flow regimes on earth, apparently have a shell shape that is not finely tuned to that environment. If this is indeed true, the shape of limpet shells provides a case study illustrating the limits to optimization through natural selection and the consequences when competing selective factors operate on the same structure.

Limits to optimization

Before examining the limits to optimization, it is necessary to show that limpets' shell shape is indeed adaptive. Although definitive proof awaits further research, there are two lines of evidence that shell shape in limpets is not merely a result of genetic drift or phylogenetic baggage. First, conical shells have evolved independently at least twice in the Patellogastropoda (D. R. Lindberg, personal communication), and strikingly similar shapes have evolved in several other wave-swept molluscan lineages (the keyhole limpets, siphonarian limpets, slipper limpets and abalones). Given this convergence, it seems safe to assume that the limpet-like shape is adaptive in the habitats where these organisms evolved.

Second, although extant snails with typical coiled shells are present on wave-swept shores, they are characteristically confined to sheltered microhabitats or are sufficiently mobile to be able to hide when the tide is in and the surf is up. This confinement is probably due to the combination of a low adhesive strength and a shell that incurs a high lift force. For example, Miller (1974) found that, for those snails that inhabit

rocky substrata, the mean tensile tenacity was 0.06±0.03 MPa (mean ± S.D., N=21). This is less than a quarter of the tenacity typical of limpets (0.28 MPa, see above). The shape coefficients of drag for limpets and snails are similar (0.534 and 0.589, respectively; Denny, 1995), but the mean lift coefficient for snails is substantially higher than that for limpets [0.406 (N=2) *versus* 0.286±0.041 (mean ± S.D., N=15)] respectively; Denny, 1995]. Thus, it seems safe to assume that, if ancestral limpets had the low tenacity and the bluff shape of a typical snail, they could not have survived while exposed to surf-zone flows. Again, this suggests that the shape of extant limpet shells is at least in part an adaptive response to life in a rapidly moving fluid.

It is possible, then to paint a scenario in which hydrodynamic forces are the primary selective factor in the evolution of limpets towards a more conical shell. Are there limits to how far selection by hydrodynamics can guide a shell towards an optimum? In answering this question, it is important to note that hydrodynamic forces would also have selected for a more tenacious foot, and the evolution of shell shape and adhesive tenacity would have proceeded hand in hand. For example, a conical shell provides a much better 'platform' from which to hang the musculature of a stiff, adhesive foot than does a typical, coiled snail's shell.

Evolution in shape and tenacity need not have occurred at the same rate, however. If, by chance, a variant arose in which the organism's adherence to the substratum was substantially increased, it would result in a concomitant decrease in the selective pressure on shell shape. Given the exceptionally high adhesive strength of most extant limpets, this seems to have been what happened. At some point, limpets became adherent enough effectively to remove hydrodynamic forces as a selective factor on shell shape. As a result, subsequent evolution of shell shape had 'permission' from the flow environment to respond to selective factors unrelated to hydrodynamics.

Furthermore, adhesive strength in limpets is, at least in part, under behavioral control. Limpets are substantially less tenacious when moving (Miller, 1974; Denny and Blanchette, 2000), but are less likely to move when wave-induced velocities are high (Judge, 1988; Wright, 1978). Thus, it is possible for a limpet to adjust its behavior to cope with a shell shape that is less than ideal. I do not mean to imply that behavior can shield shell shape from all selection by hydrodynamics (if a limpet must decrease its foraging time to accommodate a high-lift shell, its growth and reproductive output may suffer), but behavior may serve to buffer the direct effects of hydrodynamic forces on limpet mortality.

Finally, there are certain aspects of shell shape that are virtually removed from selection even when hydrodynamic forces are capable of causing mortality. Denny (1989) reports on a limpet shell (*Lottia pelta*) in which the drag coefficient was reduced by 40 % relative to its conspecifics. The changes in shell shape that led to this exceptionally low-drag morphology were subtle and incurred no apparent cost. Why, then, do not all *L. pelta* have this streamlined shape? The answer seems to be that the shape that decreases drag does not produce a concomitant decrease in lift, and in nature lift is the force most likely to be responsible for dislodging the animal from the substratum. Therefore, slight changes in shell shape that can reduce drag are unlikely to have any practical selective advantage.

Thus, the measurements reported here suggest that adhesive tenacity and shell morphology have co-evolved in limpets, resulting in a shell shape that (in a hydrodynamic sense) is 'good enough,' but not optimal. The actual shape of limpet shells is substantially shifted from that we would predict on the basis of hydrodynamics alone, from which we can infer that the evolution of shell morphology has been affected by factors other than hydrodynamics. It seems likely that there are at least five such possible factors.

First, the shape of the shell may affect the ability of the limpet to resist desiccation stresses (Branch, 1981). A high-spired shell has a small circumference relative to the volume enclosed by the shell. The primary site of evaporation from a limpet's body is at the shell's periphery, with the result that a high-spired species should lose less water per unit time (relative to its body volume) than a low-spired species. Thus, desiccation stress should act in concert with hydrodynamics to select for shells that are higher-spired that those typically found. The efficacy of this argument is questionable, however. For example, Wollcott (1973) has shown that the ability of limpets to resist desiccation is likely to be due primarily to behavioral adaptations and the presence or absence of a mucus 'curtain' at the edge of the shell. Shell shape may be less important and, as we have seen, most limpets are not particularly high-spired. It seems unlikely, therefore, that desiccation has played an important general role in the evolution of shell shape.

Second, the role of thermal stress in selecting shell shape is not clear. Branch (1981) argues that, when the sun is near the zenith above a horizontal limpet, the surface area over which direct solar radiation is absorbed by a conical shell is independent of the height-to-radius ratio of the shell, while the area available for re-radiation increases with increasing peakedness. Thus, high-spired shells should come to thermal equilibrium at a lower temperature than low-spired shells when direct solar radiation is the dominant source of thermal energy. In contrast, the temperature of a limpet may be controlled by the rate at which heat absorbed from the sun can be conducted to the cool rock beneath the foot. In this case, a low-spired shell (with a large aperture area relative to body volume) may have an advantage.

Third, high-spired shells may be more vulnerable to predation. For example, crabs can break the shell of a high-spired limpet such as *Lottia pelta* by grasping the sides of the shell at the level of the muscle attachment and squeezing. As a result, the top of the shell 'pops off', and the limpet's body is exposed (Morris et al., 1980). A similar effect is reported for tropical limpets (Lowell, 1986). A crab attempting to grasp a low-spired limpet may find that it cannot get a purchase on the sloped sides of the shell. In this case, crabs must resort to chipping away the edge of the shell (Lowell, 1986), a process

that may be more time- and energy-consuming. It seems possible, therefore, that predation has served to 'fine-tune' the shape of limpets' shells within the boundaries set by hydrodynamics and adhesion.

Fourth, in some species, there may be behavioral reasons for the anterior displacement of the apex, an effect that would be selected against by hydrodynamics. For example, *Lottia gigantea* is territorial and quite pugnacious (Stimson, 1970). In this species, the apex is displaced far to the anterior (resulting in a high lift coefficient relative to most limpets; Denny, 1995) and is used as a bulldozer by *L. gigantea* in its aggressive encounters with mussels, barnacles and other limpets in its territory. Apparently the advantage of possessing a bulldozer is sufficient to offset the slight disadvantage of high lift (see Denny and Blanchette, 2000).

Finally, D. R. Lindberg and W. F. Ponder (in preparation) suggest that a low-spired shell offers increased room in the pallial cavity, enabling a limpet to accommodate a larger gill. In areas of decreased oxygen availability (for example, in the intertidal zone at low tide when the gills are immersed in the static volume of water retained in the mantle cavity), this increased gill size may lead to increased survival.

In summary, the measurements reported here suggest that hydrodynamic lift and drag may have been important selective factors in the evolution of a conical shell in limpets, but (despite the extreme severity of the flow environment) hydrodynamic forces have not resulted in the evolution of a shell with optimal shape.

List of symbols

A_{pl}	planform area
A_{pr}	profile area
ΔA	control area for one node
AP	apex
B_{shear}	non-dimensional risk due to shear
$B_{tension}$	non-dimensional risk due to tension
C_D	drag coefficient
C_L	lift coefficient
CP	center of lift
D	drag
ΔD	drag associated with ΔA at a grid node
d_a	distance to apex
E	fractional distance to apex
ΔF	force associated with ΔA at a grid node
$\boldsymbol{g}$	acceleration due to gravity
H	shell height
i	column index for nodes
j	row index for nodes
k	height-to-radius ratio
L	lift
ΔL	lift associated with ΔA at a grid node
L_g	gross lift
M	net moment
M_D	moment due to drag
M_L	moment due to lift
$p(i,j)$	pressure at a grid node
p_b	average basal pressure
p_d	dynamic pressure
Q	lateral lift
ΔQ	lateral lift associated with ΔA at a grid node
R	shell radius
Re	Reynolds number
S	manometer deflection
T	tensile force required to resist moments
T_{act}	actual tensile force
u	water velocity
W	width of shell
$x(i)$	location of a grid node on the x axis
x_{dc}	location of the center of drag on the x axis
x_{lc}	location of the center of pressure on the x axis
Δx	spacing of grid nodes on the x axis
$y(i)$	location of a grid node on the y axis
y_c	characteristic length, here equal to λ
y_L	lift moment arm (y_{lc}–R)
y_{lc}	location of the center of pressure on the y axis
Δy	spacing of grid nodes on the y axis
$z(i,j)$	height of shell at a grid node
z_{dc}	location of the center of drag on the z axis
θ	angle of manometer from the horizontal
λ	length of shell in direction of flow
ν	kinematic viscosity
ρ	fluid density
ρ_{air}	density of air
ρ_{eff}	effective density
σ	tensile stress on basal adhesive
σ'	normalized tensile stress
σ_b	breaking stress
τ	shear stress on basal adhesive
τ'	normalized shear stress

I thank D. R. Lindberg for access to the limpet collection at the University of California Museum of Paleontology and K. Denny for assistance with the measurements of peakedness. The manuscript has benefited from the comments of D. Lindberg, L. Hunt, B. Gaylord, C. Blanchette, E. Nelson, J. Nelson and B. Hale. This research was funded by NSF Grant OCE 9115688.

References

Batchelor, G. K. (1967). *An Introduction to Fluid Dynamics.* Cambridge: Cambridge University Press.

Branch, G. M. (1981). The biology of limpets: physical factors, energy flow and ecological interactions. *Oceanogr. Mar. Biol. Annu. Rev.* **19**, 235–380.

Branch, G. M. and Marsh, A. C. (1978). Tenacity and shell shape in six *Patella* species: adaptive features. *J. Exp. Mar. Biol. Ecol.* **34**, 111–130.

Denny, M. W. (1985). Wave forces on intertidal organisms: a case study. *Limnol. Oceanogr.* **30**, 1171–1187.

Denny, M. W. (1988). *Biology and the Mechanics of the Wave-Swept Environment.* Princeton: Princeton University Press.

Denny, M. W. (1989). A limpet shell that reduces drag: laboratory demonstration of a hydrodynamic mechanism and an exploration of its effectiveness in nature. *Can. J. Zool.* **67**, 2098–2106.

Denny, M. W. (1993). *Air and Water*. Princeton: Princeton University Press.

Denny, M. W. (1995). Predicting physical disturbance: mechanistic approaches to the study of survivorship on wave-swept shores. *Ecol. Monogr.* **65**, 371–418.

Denny, M. W. and Blanchette, C. A. (2000). Hydrodynamics, shell shape, behavior and survivorship in the owl limpet *Lottia gigantea*. *J. Exp. Biol.* **203**, 2623–2639.

Denny, M. W., Daniel, T. L. and Koehl, M. A. R. (1985). Mechanical limits to size in wave-swept organisms. *Ecol. Monogr.* **55**, 69–102.

Denny, M. and Gaylord, B. (1996). Why the urchin lost its spines: hydrodynamic forces and survivorship in three echinoids. *J. Exp. Biol.* **199**, 717–729.

Gaylord, B. (1997). Consequences of wave-induced water motion to nearshore macroalgae. PhD thesis, Stanford University, Stanford, California.

Gaylord, B. (2000). Size, scaling and compliant design in intertidal organisms: implications of fine-scale features of surf-zone flow. *Limnol. Oceanogr.* **45**, 174–188.

Grenon, J.-F. and Walker, G. (1981). The tenacity of the limpet, *Patella vulgata* L.: an experimental approach. *J. Exp. Mar. Biol. Ecol.* **54**, 277–308.

Hahn, T. and Denny, M. W. (1989). Bird predation, adhesive tenacity and the spatial distribution of limpets. *Mar. Ecol. Progr. Ser.* **53**, 1–10.

Judge, M. L. (1988). The effects of increased drag on *Lottia gigantea* (Sowerby 1834) foraging behaviour. *Funct. Ecol.* **2**, 363–369.

Lindberg, D. R. (1981). Acmaeidae. In *Invertebrates of the San Francisco Bay Estuary System* (ed. W. Lee), pp. 52–100. Pacific Grove, CA: Boxwood Press.

Lowell, R. B. (1985). Selection for increased safety factors of biological structures as environmental unpredictability increases. *Science* **228**, 1009–1011.

Lowell, R. B. (1986). Crab predation on limpets: predator behavior and defensive features of the shell morphology of the prey. *Biol. Bull.* **171**, 577–596.

Lowell, R. B. (1987). Safety factors of tropical *versus* temperate limpet shells: multiple selection pressures on a single structure. *Evolution* **41**, 638–650.

MacPherson, J. H. (1955). Preliminary revision of the families Patellidae and Acmaeidae in Australia. *Proc. R. Soc. Victoria* **67**, 229–256.

Miller, S. L. (1974). Adaptive design of locomotion and foot form in prosobranch gastropods. *J. Exp. Mar. Biol. Ecol.* **14**, 99–156.

Morris, R. H., Abbott, D. P. and Haderlie, E. C. (1980). *Intertidal Invertebrates of California*. Stanford: Stanford University Press.

Ponder, W. F. and Creese, R. (1980). A revision of the Australian species of *Notoacmea*, *Collisella* and *Patelloida* (Mollusca: Gastropoda: Acmaeidae). *J. Malac. Soc. Australia* **4**, 167–208.

Schey, H. M. (1973). *Div, Grad, Curl and All That.* New York: W. W. Norton, Co.

Schlichting, H. (1977). *Boundary Layer Theory.* New York: McGraw-Hill.

Stimson, J. (1970). Territorial behavior of the owl limpet, *Lottia gigantea*. *Ecology* **51**, 113–118.

Vermeij, G. J. (1993). *A Natural History of Shells.* Princeton: Princeton University Press.

Vogel, S. (1994). *Life in Moving Fluids.* Second edition. Princeton: Princeton University Press.

Warburton, K. (1976). Shell form, behavior and tolerance of water motion in the limpet *Patina pellucida* (L.) (Gastropoda: Prosobranchia). *J. Exp. Mar. Biol. Ecol.* **23**, 307–325.

Wollcott, T. G. (1973). Physiological ecology and intertidal zonation in limpets (*Acmaea*): a critical look at ‘limiting factors’. *Biol. Bull.* **145**, 389–422.

Wright, W. G. (1978). Aspects of the ecology and behavior of the owl limpet, *Lottia gigantea* Sowerby, 1834. *West. Soc. Malacol. Annu. Rep.* **11**, 7.